

Research



**Cite this article:** Fagereng Å, Beall A. 2021 Is complex fault zone behaviour a reflection of rheological heterogeneity?. *Phil. Trans. R. Soc. A* **379**: 20190421.  
<https://doi.org/10.1098/rsta.2019.0421>

Accepted: 18 August 2020

One contribution of 7 to a discussion meeting issue 'Understanding earthquakes using the geological record'.

**Subject Areas:**

geology, geophysics, plate tectonics

**Keywords:**

faults, shear zones, rheology, earthquakes, creep

**Author for correspondence:**

Å. Fagereng  
e-mail: [fagerenga@cardiff.ac.uk](mailto:fagerenga@cardiff.ac.uk)

# Is complex fault zone behaviour a reflection of rheological heterogeneity?

Å. Fagereng and A. Beall

School of Earth and Ocean Sciences, Cardiff University, Park Place, Cardiff CF10 3AT, UK

 ÅF, 0000-0001-6335-8534

Fault slip speeds range from steady plate boundary creep through to earthquake slip. Geological descriptions of faults range from localized displacement on one or more discrete planes, through to distributed shearing flow in tabular zones of finite thickness, indicating a large range of possible strain rates in natural faults. We review geological observations and analyse numerical models of two-phase shear zones to discuss the degree and distribution of fault zone heterogeneity and effects on active fault slip style. There must be certain conditions that produce earthquakes, creep and slip at intermediate velocities. Because intermediate slip styles occur over large ranges in temperature, the controlling conditions must be effects of fault properties and/or other dynamic variables. We suggest that the ratio of bulk driving stress to frictional yield strength, and viscosity contrasts within the fault zone, are critical factors. While earthquake nucleation requires the frictional yield to be reached, steady viscous flow requires conditions far from the frictional yield. Intermediate slip speeds may arise when driving stress is sufficient to nucleate local frictional failure by stress amplification, or local frictional yield is lowered by fluid pressure, but such failure is spatially limited by surrounding shear zone stress heterogeneity.

This article is part of a discussion meeting issue 'Understanding earthquakes using the geological record'.

## 1. Introduction

Faults are classically thought to creep steadily or slip episodically in earthquakes, with more complex conceptual models involving seismogenic patches embedded within otherwise aseismic faults [1–4]. It is, however, now clear that faults slip at a continuum of speeds [5]. Here, we review and discuss this slip rate continuum in the context of geological fault zone structure.

## 2. Depth-dependency of fault zone structure, strength and frictional stability

A now classic model of fault zone structure describes an upper brittle zone governed by pressure-dependent frictional sliding above a deeper ductile zone with grain-size and/or temperature-dependent viscous rheology [6–8] (figure 1*a,b*). Geologically, the upper, frictional regime is characterized by brittle fault rocks, including gouges, cataclasites and pseudotachylytes (lithified friction melt), where one or more discrete fault cores are surrounded by a fractured damage zone [2,10]. The deeper, viscous regime is characterized by mylonites, defined as recrystallized and/or neocrystallized rocks, commonly with relatively thin (cm-m), anastomosing higher strain zones within a broad (>km) foliated shear zone [11–13]. The shallower and deeper fault rocks reflect a well-recognized crustal strength profile, where frictional strength increases with increasing normal stress, and viscous strength decreases with increasing temperature [7]. The frictional–viscous transition is defined where the shear stresses ( $\tau$ ) driving frictional and viscous deformation are equal for some given strain-rate, composition, stress regime and thermal gradient. In reality, this depth is going to be a broad zone where both frictional and viscous deformation mechanisms are active [14,15]. Note that we have here defined ‘brittle’ and ‘ductile’ as descriptive terms for macroscopically localized and distributed deformation, respectively. ‘Frictional’ and ‘viscous’, respectively, refer to mechanisms where shear stress is proportional to normal stress and shear strain rate. We avoid the term ‘plastic’, but recognize that what we describe as ‘viscous’ deformation will have an activation energy.

The geological and mechanical observations outlined above for a homogeneous fault zone relate to, but do not fully describe, the fault’s depth-dependent seismic behaviour. This is further described by velocity-dependence of friction, denoted by the parameter ( $a - b$ ), defined by  $\tau = \sigma'_n[\mu^* + (a - b)\log(V/V^*)]$  in the steady-state form of the rate and state friction law [9,16–20] (figure 1*c*). Here,  $\mu^*$  is the coefficient of friction at reference velocity  $V^*$ ,  $\sigma'_n$  is effective normal stress and  $V$  is slip velocity. In this framework, velocity-strengthening faults (where  $(a - b) > 0$ ) accommodate displacement by stable, steady sliding, because slip does not accelerate after nucleation. Note that  $(a - b)$  can vary with velocity [21–24], and evolve as fault rocks develop [25,26], and ruptures can therefore propagate within steady-state stable regimes under some conditions [27–29]. Velocity-weakening faults (where  $(a - b) < 0$ ) are unstable if the critical stiffness ( $k_c$ ), a threshold that depends on material properties and effective normal stress, exceeds the system stiffness ( $k$ ), determined by the wallrock stiffness. Unstable fault patches can generate earthquakes under static loading. Conditional stability occurs when  $(a - b) < 0$  and  $0 < k_c < k$ . Note that  $k$  decreases as a slipping region grows, such that conditionally stable fault patches can be destabilized as they reach a critical length scale known as the nucleation length [9]. Conditionally stable areas cannot nucleate earthquakes without a dynamic load, but earthquakes may propagate into a conditionally stable field if the dynamic velocity step is sufficient. This framework infers that rocks in the deep viscous regime are velocity-strengthening because of the stable sliding observed there, and predicts that stable sliding prevails at very shallow depths where poorly lithified rocks accommodate displacement by granular flow involving dilatancy-hardening [30]. The seismogenic zone, where earthquakes can nucleate, covers a depth range between these shallow and deep aseismic, stably sliding zones. Several experiments have correlated the seismogenic zone, defined as where steady-state frictional sliding is potentially unstable, with temperatures in the range 100–350°C in quartzofelspathic rocks [31] and phyllosilicate-rich gouges [32,33]; similar to thermal constraints determined from combining thermal models and the depth-distribution of seismicity [34,35]. The seismogenic zone

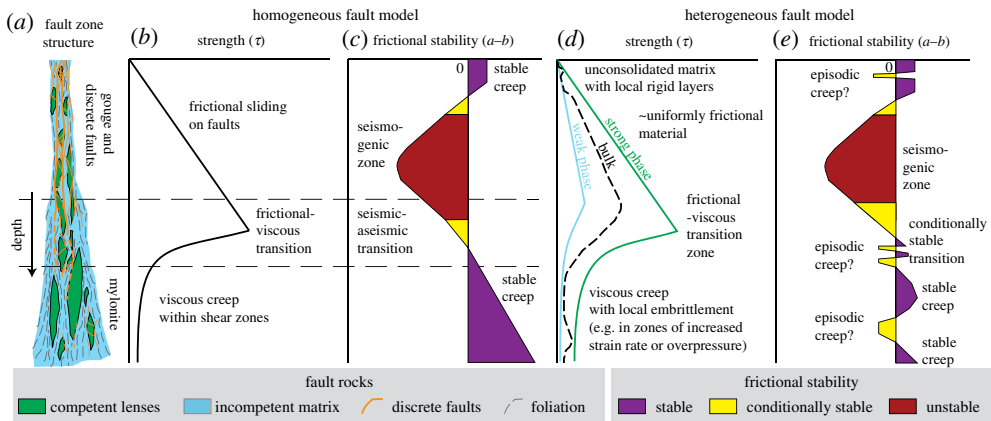


**Figure 1.** The generalized structural model of a fault zone, here shown for a vertical fault (*a*), illustrates a dominantly brittle regime of discrete faults within a wider damage zone underlain by a dominantly ductile regime where shear is accommodated within mylonites [6]. In (*b*), the same brittle–ductile two-layer system is described by a shallower layer where frictional strength increases with depth, down to a frictional–viscous transition where viscous deformation becomes easier than frictional failure and strength decreases with increased temperature and pressure [7]. (*c*) Illustrates that the transition between shallow frictional failure and deeper viscous creep may also be comparable to depth-dependent changes in steady-state frictional stability [9]. The models in (*b*) and (*c*) are simplified, and assume a homogeneous lithology subject to constant stress and strain rate. When more complexity is included, variations thereof are more appropriate, as shown by examples in (*d*) and (*e*). (Online version in colour.)

is considered separated from the stably sliding zones above and below by transitional regimes of conditional stability [9,19] (figure 1*c*).

In transitional, conditionally stable regimes, slip speeds intermediate between steady creep and earthquakes have now been observed globally in ‘slow earthquakes’, a term that includes slow slip and low frequency earthquakes. ‘Slow slip events’ (SSEs) have been observed geodetically in well-instrumented plate boundary zones across the globe over the last two decades, and represent episodes of transient creep that repeat near-periodically at rates of mm to cm per day [36,37]. Low frequency earthquakes (LFEs) are energetic pulses depleted in high frequencies, relative to ordinary earthquakes, and represent plate boundary shear displacement [38,39]. LFEs are commonly spatially and temporally associated with SSEs in ‘episodic tremor and slip’ (ETS) events, when slow slip is accompanied by persistent, low frequency seismic signals that comprise swarms of LFEs [40–42]. Slow earthquakes have now been observed at depths from no more than a few kilometres below the sea floor in Japan and New Zealand [43,44], to as much as 90 km in the Alaskan subduction zone [45]. Thus, there is no distinct pressure ( $P$ ) or  $T$  regime associated with slow earthquakes, but they do seem associated with conditional stability at or close to the seismic–aseismic transition [20,46,47].

### 3. Geological observations of fault zone heterogeneity

Generalized, 1-D homogeneous fault models (figure 1*a–c*) assume a single composition with a single depth-dependent rheology. Our aim here is to analyse the effect of rheological heterogeneity on the bulk behaviour of fault and shear zones—with focus on how strength contrasts between coexisting materials determine the depth range of the frictional–viscous transition, and potential consequences for seismic, aseismic, and intermediate behaviours.

#### (a) Fault zone heterogeneity at shallow depths

Subduction-related mélanges commonly preserve evidence for early, soft sediment deformation structures overprinted by later faults and fractures [48,49] (figure 2*a*). A common interpretation

is therefore that subduction plate interface deformation style progressively changes from near-trench distributed, ductile deformation of unconsolidated sediments to localized, frictional sliding along faults in sedimentary rocks as the strata consolidate and lithify with progressive displacement and burial [50,54–56]. Accordingly, a shallow updip limit of earthquake nucleation in subduction zones has been associated with low-temperature diagenetic processes [57,58]. The transition from macroscopically ductile to brittle deformation occurs, however, at different conditions in different materials. This is clear where sandstone boudins contain fractures that do not continue into surrounding mudstone matrix (figure 2*b*). There is therefore a depth range, between shallow unconsolidated sediments and deeper consolidated rocks, where variable states of consolidation is an important source of heterogeneity.

Both strike-slip faults and subduction-related thrusts show variable sliding characteristics and heterogeneous interseismic accumulation of elastic strain at shallow depths [43,44,59–61]. Like the progressive and potentially heterogeneous consolidation observed in exhumed mélanges (figure 2*a,b*), the geophysical observations in active faults question the model of uniformly velocity-strengthening, unconsolidated sediments (figure 1*c*). An adaptation of the conceptual model is that shallow instabilities can be generated by one or more layers of frictionally unstable material within the frictionally stable zone (figure 1*e*). Such layers have been inferred to generate episodic creep in southern California, where relatively strong shallow intrusions and more lithified strata are inferred within otherwise unconsolidated or clay-rich velocity-strengthening fault rocks [62] (figure 1*d,e*). Similarly, in the Hikurangi subduction margin, highly variable input sediments are hypothesized to play a part in shallow SSEs [63,64].

That fractures are limited to a single material (as in figure 2*b*) implies that the brittle yield is not met on both sides of the bimaterial interface. Lack of fracture propagation from one material to another also implies that the static stress drop in the ductile deformed matrix (potentially lowered by a viscously relaxed background stress) was insufficient to overcome frictional resistance, such that unstable slip was limited in dimension by the extent of relatively rigid materials. Fractures may also have been arrested prior to reaching instability if they are constrained to blocks that are smaller than a critical length scale [65]. Where shallow subduction-related thrusts have been drilled and sampled, there is evidence for both brittle and ductile deformation [66–68], also where lithological variation is not obvious [69]. Thus, local variation in deformation mode can occur without compositional heterogeneity, for example in conditionally stable regions that, over time, experience both unstable and stable deformation, because other factors, such as porosity or fluid pressure, can vary in time and space and affect frictional stability [70–72].

## (b) Heterogeneity in the seismogenic zone

The earthquake cycle has long been recognized as resulting from elastic rebound [73], where a new or existing fault accommodates stick-slip motion [74]. In this conceptual model, failure occurs when local fault-parallel shear stress, resulting from wall rock elastic strain, exceeds the cohesion plus frictional resistance of the fault rocks. Numerical models of this process are limited by computational constraints, and faults are therefore commonly considered as planar, discrete surfaces [75,76]. In such models, each point on the fault is given a single set of parameters that represents that location in time and space. This is an appropriate representation of relatively thin, planar faults [10] (e.g. figure 2*c*), where slip is well approximated by lateral interaction between segments of a single continuous fault. However, many fault zones are volumetric features [77], where fault-normal heterogeneities and interactions must also be considered.

Tabular faults that contain one or more discrete fault planes in a broad zone of foliated, viscously deforming matrix can, on the other hand, deform by a combination of distributed viscous flow of the matrix and localized frictional failure along or within more competent lenses [2,78] (e.g. figure 2*d*). In this scenario, viscous creep accommodates finite strain at slow strain rates over long time scales, whereas frictional failure typically occurs at episodically high strain rates over short time scales once a critical level of stress has been reached [79,80], although

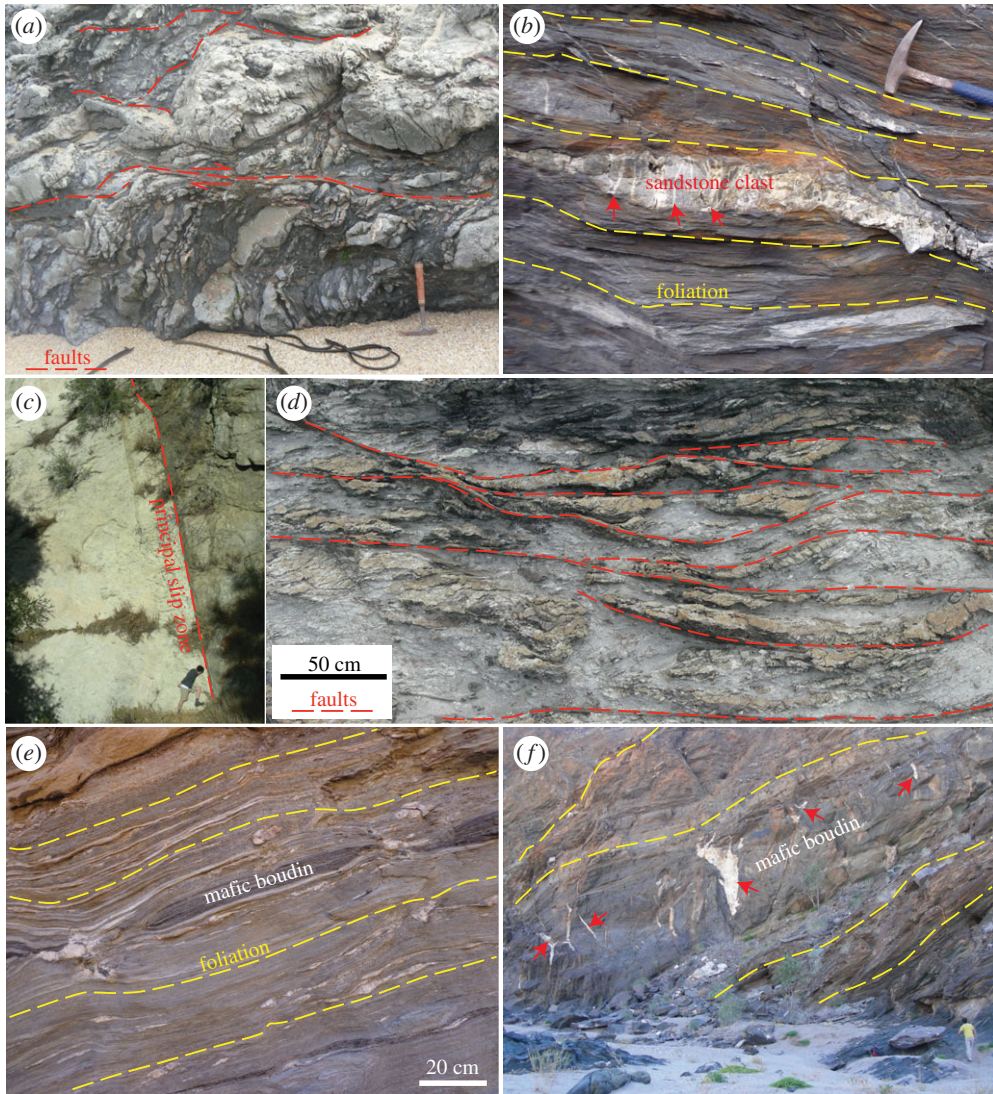


**Figure 2.** Photographs illustrating examples of lithological heterogeneity linked to deformation style, at a range of depths. In (a) dismembered bedding, developed by distributed independent particle flow in poorly to un-consolidated sediments, is crosscut by a subhorizontal through-going fault (Chrystalls Beach Complex, New Zealand [50]); (b) shows an example of a sandstone layer welded by quartz-filled fractures (red arrows at examples) that do not continue into the surrounding foliated mudstone matrix (Makimine Mélange, Kyushu, Japan [51]). An example of a cm-thick, principal slip zone in crystalline rock is found in the San Gabriel fault, California (c), and contrasts with an anastomosing fault system in the Chrystalls Beach Complex (d). In shear zones exhumed from depths below the seismogenic zone, here the Kuiseb schist that deformed at temperatures in excess of 500°C [52,53], competent mafic layers are boudinaged (e) and locally fractured and faulted (red arrows in f). (Online version in colour.)

some phyllosilicates may also slide stably and frictionally at low strain rates [81]. The viscous mechanism is commonly pressure solution [80,82–84], and the rate of pressure solution will tend to vary along the fault, as it is a function of grain size, shear zone thickness, composition and other factors affecting chemical potential gradients [84–87]. Consequently, the displacement accommodated by pressure solution varies in space, resulting in along-strike and down-dip spatio-temporal variation in elastic strain energy stored in the wall rocks. Therefore, the ratio

of shear stress to bulk shear zone frictional yield strength will vary spatiotemporally both along-strike and down-dip.

In two dimensions (map-view) the seismogenic zone of a rheologically heterogeneous fault may be best represented by locked patches, which creep inefficiently, in a dominantly creeping fault zone [1,3]. One may expect locked areas to dominate (by area) in localized faults lacking evidence for a wider creeping zone (e.g. figure 2c) and creep or mixed behaviour to be common in thicker heterogeneous fault zones with scattered rigid inclusions (e.g. figure 2d). The bulk fault strength of the latter will depend on the volume fractions and geometry of two (or more) rheological components [77] (figure 1d). For fault patches where interseismic creep is too slow to accommodate tectonically imposed displacement rates, elastic strain will accumulate until failure occurs—at a strength determined by the frictional yield of locked or partially locked areas, and potentially highly influenced by fluid pressure.

### (c) Heterogeneity below the seismogenic zone

Mylonites formed deeper than the seismogenic zone are typically characterized by structures formed by distributed flow in polyphase materials, where variable viscosity is commonly illustrated by pinch-and-swell or boudinage of relatively competent layers [88–90] (figure 2e). Some relatively rigid lenses and/or layers may remain in a frictional regime while adjacent rocks deform by diffusion or dislocation creep [91,92] (figure 2f), potentially leading to an intermingling of velocity-weakening and velocity-strengthening rocks [77,93].

Progressive shear in a dominantly viscous shear zone may gradually increase stress in and around rigid bodies embedded within it, allowing a frictional yield to be reached locally and transiently [94,95]. Such frictional failure may be damped by surrounding viscous matrix [24, 96,97], although this matrix may host dynamic rupture propagation if a critical stress level is reached [29]. Heterogeneity in viscous flow will tend to decrease with depth, theoretically, as most materials weaken exponentially with increasing temperature (figure 1d). Although, local variations in metamorphic reaction progress may also increase heterogeneity at depth, either by producing stronger products along a prograde path, for example in eclogitisation, [98], or by retrograde growth of weak phyllosilicates [82,99].

Whereas viscosity contrasts are likely to exist throughout shear zones accommodating dominantly stable sliding below the seismogenic zone, there are areas where the contrasts are larger. These are regions where matrix viscosity is low, creep in competent materials is slow and bulk shear stress is well below the frictional yield strength of the stronger components. Locally, however, frictional failure may occur within more competent rocks because yield strength is lowered by high fluid pressures [100], or because stress amplification occurs by loading of rigid clasts by surrounding flowing materials [101]. This local, and probably small displacement, frictional failure within otherwise viscously creeping shear zones has been invoked to explain both regular (but deep) earthquakes [94,95] and slow earthquakes [53,97,102].

## 4. Depth-dependence of viscosity contrasts in heterogeneous faults

Our review so far highlights various sources and degrees of rheological heterogeneity as a function of depth (figure 3). From here, we will simplify the discussion by considering fault zones as containing two components—one that is less competent and deforms efficiently by distributed flow, and another that is more competent, rigid, deforms inefficiently by viscous flow and therefore tends to fracture or host frictional failure along faults. The term ‘competent’ derives from a structural geology field term, and describes the inferred rigidity of a material at the time of deformation. The two contrasting fault zone materials can therefore be thought of as having low ( $\eta_w$ ) and high ( $\eta_s$ ) viscosities at a steady creep rate, and an effective bulk viscosity describing the combined visco-brittle deformation, defined by  $\eta' = \tau/\dot{\gamma}$  where  $\dot{\gamma}$  is shear strain rate, itself defined by slip velocity divided by deforming thickness ( $v/w$ ).

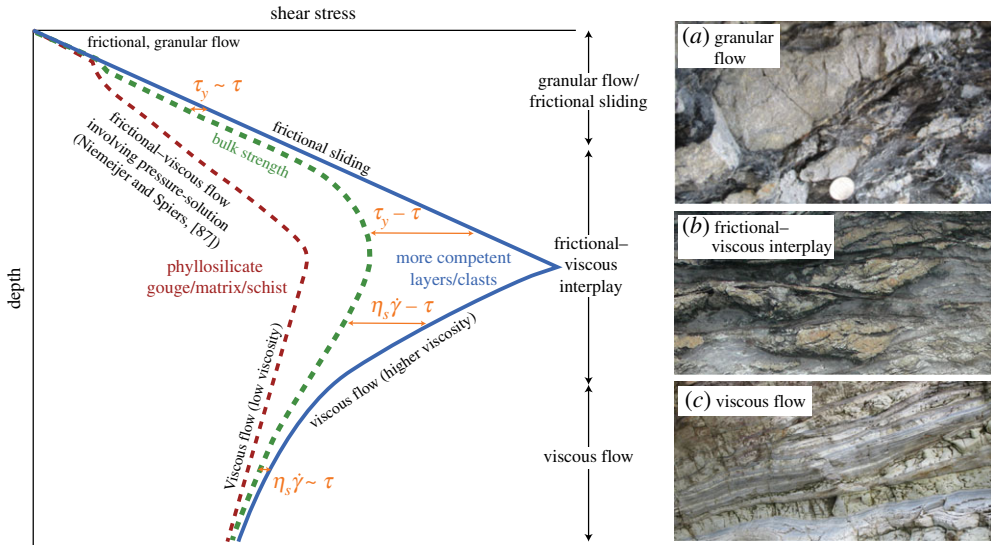


**Figure 3.** Schematic diagram showing the difference in depth-dependent strength between two components. The red, dashed curve shows a relatively weak, fine-grained phyllosilicate-rich matrix deforming preferentially by pressure solution creep. The blue, solid line represents coarser-grained layers, possibly dismembered into oblate clasts, that are too coarse for efficient pressure solution. The stress driving bulk deformation (intermediate, dashed green curve) is expected to be similar to the frictional yield strength ( $\tau \sim \tau_y$ ) in the frictional regime, and similar to the viscous strength of competent material at the imposed strain rate ( $\tau \sim \eta_s \dot{\gamma}$ ) in the viscous regime. Deviations from these conditions are associated with the frictional–viscous interplay zone. Photographs to the right show potential structures developing in this material mixture: (a) sandy layers dismembered by granular flow in a mudstone matrix (Makimine Mélange, Japan), (b) dismembered sand and chert layers in a cleaved, phyllosilicate rich matrix, cross-cut by anastomosing faults (Chrystalls Beach Complex, New Zealand), (c) layers of sheared metapelite, metapsammite, and metabasalt, with near-planar margins indicating small viscosity contrast (Makimine Mélange, Japan). (Online version in colour.)

We consider a low viscosity, phyllosilicate-rich fault zone containing rigid lenses (figure 3), as typical of many fault zones as discussed above. The competent component has a frictional yield strength that increases linearly with depth, from the surface to a depth where viscous creep can occur at the imposed strain rate. This linear increase in frictional strength does not occur where the fluid pressure follows a lithostatic gradient below a fluid retention depth; in such examples strength can be uniform and low at depths of fluid overpressure [103,104]. Conceptually, this is no different from ‘Christmas Tree’ strength profiles discussed by many authors [7]. The less competent material represents phyllosilicate-rich fault gouges, foliated matrix material in tabular fault zones, and the least competent element of micaceous schists. The plot in figure 3 is intentionally plotted with no scale, as the absolute values of shear strengths and depths will depend on rocktypes (both composition and grain size), thermal gradient, tectonic regime, strain rate, fluid pressure and other parameters. We use this conceptual plot to define three conceptual regimes.

### (a) Granular flow and/or frictional sliding

At the shallowest depths the rheology is granular flow and/or frictional sliding, with possible effect of pressure solution. In sheared sedimentary sequences, the typical observation is dismembered sandy layers in a muddier matrix (figure 3a); however, one can think more generally of stronger layers dismembered in a weaker matrix, where strength is defined as the frictional yield  $\tau_y = C_0 + \mu(\sigma_n - P_f)$ . Here,  $C_0$  is cohesion and  $\mu$  is static coefficient of friction, such that both level of consolidation/cementation and frictional properties determine relative strengths.

This means that both composition and consolidation state is important, and relative strength may vary, and locally invert, as sedimentary layers undergo diagenesis at different rates [105]. Friction is typically velocity-strengthening at these shallow depths [30,31,106].

### (b) Frictional–viscous interplay

At depths where rocks are consolidated, faulting is typically governed by some combination of pressure-solution and frictional sliding [80,86,87,107]. The conceptual strength curve for phyllosilicate-rich gouges (figure 3) follows a frictional–viscous flow for a micaceous matrix with soluble, rigid inclusions [86,87]. Deeper than a depth determined by the temperature where pressure solution becomes effective, roughly 100–150°C for quartz [108,109], the phyllosilicate-rich gouge will be able to creep at a stress lower than the frictional yield strength of the stronger component. If pressure solution is less efficient, for example because grain size is large, strain rate is high, or rocks are relatively dry, this will be a regime where rates of pressure solution and frictional granular flow are comparable. At such conditions of competition between granular flow and pressure solution at steady state, faults are velocity-weakening and potentially seismogenic [23,80,110–113]. Various combinations of creep and stick-slip will exist depending on spatial and temporal distribution of viscous and frictional deformation, as was discussed in §3(b) and is illustrated by local through-going faults within a shear zone of competent clasts in a foliated matrix in figure 3*b*. The highest degree of visco-frictional interaction is predicted at depths just below the competent material's frictional–viscous transition, where both the frictional yield ( $\tau_y$ ) and the viscous strength of component material at the imposed strain rate ( $\eta_s \dot{\gamma}$ ) are too high for either uniform frictional sliding or viscous flow to occur (figure 3).

### (c) Viscous flow

Deeper than the frictional–viscous transition of the more competent phase, the flow strengths of both materials are less than the frictional yield of the more rigid fault rocks at the steady-state strain rate. Therefore, below the frictional–viscous transition in the competent phase, the bulk flow stress departs significantly from the frictional yield curve. For shear stress to locally reach frictional yield strength at these depths, one of two things must happen; either the stress increases (for example by local stress amplification caused by the flowing matrix; [94,95,101]) or frictional yield decreases (for example by local increase in fluid pressure). In this regime, the viscosity contrast decreases with increasing depth and temperature, and can become very small if both components flow viscously at small driving stresses ( $\tau \sim \eta_s \dot{\gamma} \sim \eta_w \dot{\gamma}$ ; figure 3*c*).

## 5. Modelled effects of rheological heterogeneity on slip behaviour

To further analyse the effects and importance of rheological heterogeneities as described above from the geological record, we take a conceptual approach to modelling two-phase shear zones. Previous numerical studies have also considered effects of heterogeneity on fault zone behaviour. For example, by considering brittle asperities in a viscous matrix representing the seismic–aseismic transition at the base of the subduction megathrust seismogenic zone [114], by alternating velocity-weakening and velocity-strengthening properties in a rate-and-state dependent formulation of fault friction [96,115], or by varying pressure solution kinetics within seismic cycle simulations incorporating a microphysical model [29]. Another approach has been to simulate slow slip transients as initiated by local fracture [116]. Slip rate transients can also arise from interaction between competent clasts in a weak matrix [117], an interaction that also creates local stress amplification [101].

## (a) Method

Using the particle-in-cell finite element code Underworld [118], we compute velocity and pressure fields for a two-dimensional cross section, assuming plane strain, of a shear zone containing more viscous elliptical clasts in a less viscous matrix [97,101]. Both clasts and matrix follow a Newtonian, linear viscosity, but clasts also have a frictional yield strength  $\tau_y$  dictated by the Mohr–Coulomb failure criterion. This set-up is analogous to matrix deformation by pressure solution, with embedded, higher viscosity clasts that may flow slower than the matrix, or episodically fracture in response to locally amplified stresses or a low frictional yield strength [97]. Dynamic frictional slip is not modelled. All results can be non-dimensionalized and scaled [101], such that the only model variables are the viscosity ratio of the strong and weak components,  $\eta_s/\eta_w$ , and the ratio of driving stress to frictional yield  $\tau/\tau_y$ . Periodic boundary conditions are applied to the left- and right-hand boundaries, the base is kept stationary and a constant driving shear stress,  $\tau$ , is applied to the top boundary. The model domain has a 4 : 1 aspect ratio and a high mesh resolution of  $2048 \times 512$  is used to resolve the anastomosing matrix. The shear zone contains 61% competent clasts, to simulate an anastomosing shear zone system, and these clasts have a power-law size distribution with a constant aspect ratio of 1 : 3 and a maximum long axis of 84% shear zone thickness. We explore how clast fracturing and shear zone strain-rate heterogeneity depend on varying  $\eta_s/\eta_w$  and  $\tau/\tau_y$ . Note that because stresses are amplified by the stronger clasts, local stresses will exceed the applied driving stress [101]. Models with  $\eta_s/\eta_w = 10^3$  have been described in [101], where more detail on the modelling procedure is available. Additional models with  $\eta_s/\eta_w = 10$  and  $10^2$  were run for this study.

The aim here is not to model specific faults, conditions, scales or settings, but to consider a fault system where interconnected weak zones between more competent lenses may allow strain localization, while we can also assess how deformation is distributed between the two phases and how the fault zone behaves as a bulk aggregate. We are interested in how the ratios  $\eta_s/\eta_w$  and  $\tau/\tau_y$  influence the likelihood that a chain of adjacent clasts will have stress states at frictional failure, which is assumed to be analogous to bulk shear zone frictional failure. The former ratio represents the degree of viscous heterogeneity. The latter ratio is also a measure of heterogeneity, because  $\tau/\tau_y \rightarrow 1$  will mean that the fault zone is essentially at brittle failure,  $\tau/\tau_y \ll 1$  represents a bulk viscous shear zone, but  $0 < \tau/\tau_y < 1$  can lead to intermediate behaviours. Considering the ratio  $\tau/\tau_y$  is not new—it is an inverse form of the engineering safety factor for slope stability [119], analogous to a flow factor that can control slow versus rapid sediment mass transport [120], and similar ratios describe on-fault frictional deformation versus off-fault ductile matrix flow in experiments [121]. Note that several other factors, such as the clast:matrix ratio, the size, aspect ratio, and size distribution of clasts, and thickness of the shear zone, will also affect the model results—however, these parameters will affect absolute values rather than the general trends, and it is the general trends we wish to discuss here.

## (b) Effects of variable viscosity ratio and $\tau/\tau_y$

First consider a model with a high viscosity ratio,  $10^3$  (figure 4). Such high viscosity ratios are most likely above or slightly below the frictional–viscous transition in the competent phase, in areas of local hydration and alteration to weak minerals, at shallow depths where consolidation is highly variable, or other settings where low viscosity materials encompass competent lenses.

The large viscosity contrast will lead to local strain rate gradients that induce amplified shear stresses in the competent clasts [101], as also predicted for rigid inclusions in both elastic and plastic systems in the absence of clast interaction [122,123]. At driving stress near the frictional yield,  $\tau/\tau_y = 0.88$ , this stress amplification is sufficient for 99% of total clast volume to be at frictional failure (figure 4a). Because fracturing is now essentially occurring throughout the competent clasts, while the matrix is flowing easily, the aggregate is deforming at a more or less constant strain rate (figure 4b). Though dynamic frictional slip is not modelled, we can hypothesize how such slip would be affected by the static stress state calculated here, by

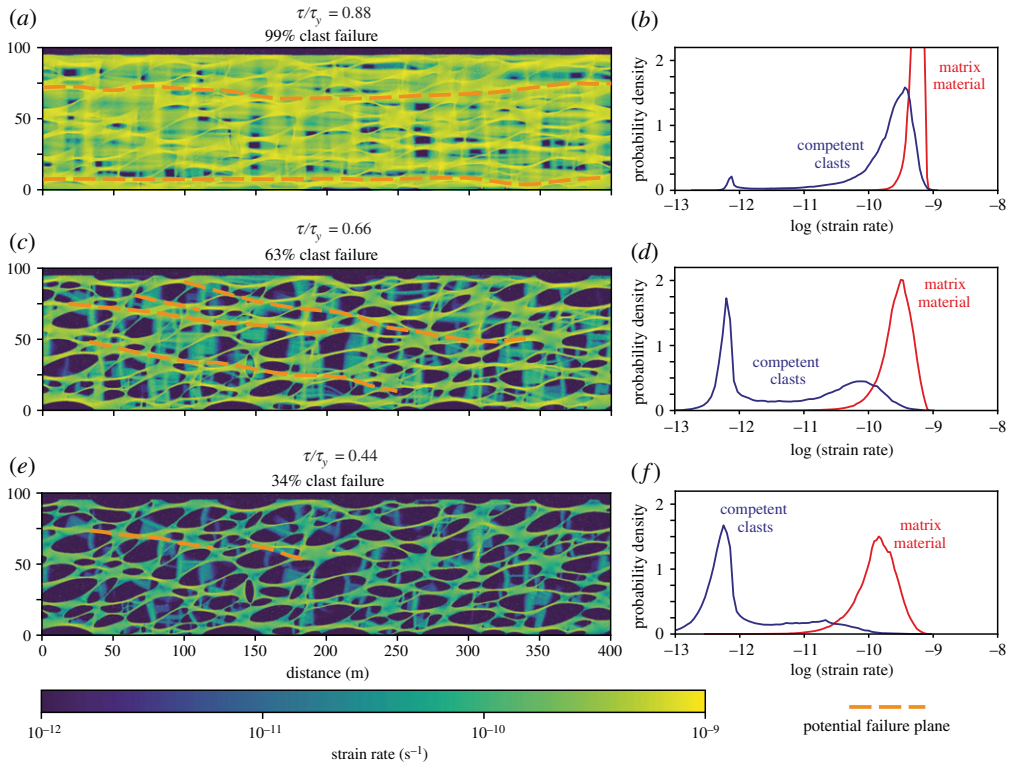


**Figure 4.** Plots of strain rate distribution within a linear-viscous shear zone, where the viscosity ratio between clasts and matrix is  $10^3$ . Models are run at different ratios of driving stress ( $\tau$ ) to frictional yield stress ( $\tau_y$ ) of the competent phase. When  $\tau/\tau_y$  approaches 1 (a), frictional deformation dominates and allows uniformly high strain rates (b). Compare this to a small  $\tau/\tau_y$  where only  $\sim 1/3$  of clast volume is failing frictionally (e), and the strain rates are bimodal (f), with much faster deformation in the weak, viscously flowing matrix. In the intermediate case (c), sufficient clast volume (greater than 50%) is failing to allow potential for through-going discrete fractures to form locally and transiently, linking fracturing clasts through the matrix material. In this case, the probability density distribution of strain rate (d) shows a narrow peak for clasts deforming slowly and viscously, and a broader peak for faster deformation in clasts that are undergoing some level of frictional deformation. The strain rate is given in units of  $s^{-1}$  assuming a matrix viscosity of  $10^{17}$  Pa s and  $\tau_y = 160$  MPa [97]. (Online version in colour.)

considering that earthquake ruptures can potentially propagate through velocity-strengthening patches of similar length scale [115], or that experience a background stress near their frictional yield strength [29], but will likely terminate in regions where the ambient stress is far below the yield strength [124]. In this case, all clasts are at failure and any unstable frictional slip nucleating in one clast may plausibly propagate through the shear zone and a principal slip zone may develop in such a system (figure 4a).

At an intermediate  $\tau/\tau_y$  of 0.66, 63% of clast material is at frictional yield (figure 4c). Under these conditions, the strain rate in the competent clasts covers a broad range, with a peak deforming at a slow strain rate controlled by their viscosity, and others deforming faster as fractures allow them to reach matrix strain rates (figure 4d). Though much of the clast stress distribution is lower than the frictional yield, depicted by low strain-rates, hypothesized rupture pathways could still be connected between clasts that are at frictional failure (figure 4c) as fractures dynamically overcome shear resistance and velocity-strengthening friction in the matrix. This stress field may therefore be conducive to earthquake nucleation. Note that these potential rupture planes are slightly oblique to shear zone margins and will be limited in length by the shear zone thickness. If  $\tau/\tau_y$  is lower still, 0.44, then only 34% of clasts are at frictional failure, and the fault zone is dominated by viscous flow (figure 4e); the strain rate distribution is bimodal,

with clearly different strain rates in fast flowing matrix and much slower flow in competent clasts (figure 4f). The driving stress is too low, or frictional yield strength too high, for much clast material to be at frictional failure, and the hypothesized failure planes are limited to short segments that rarely connect between multiple clasts without passing through material far from frictional failure (figure 4c). Thus, fault lengths are likely to remain shorter than the nucleation length scale for instabilities.

A viscosity ratio of  $10^3$  in summary gives a range from nearly fully frictional clast deformation if  $\tau/\tau_y$  is 0.88, through to dominantly viscous flow at  $\tau/\tau_y$  of 0.44, although about 1/3 of clast volume still fails frictionally at this stress ratio, albeit at very limited length scales. Reducing the viscosity ratio to 10 changes the picture to largely remove the intermediate frictional–viscous behaviour (figure 5). In this case,  $\tau/\tau_y = 0.88$  again leads to near total frictional behaviour, with 96% of clast material yielding, and potential for through-going failure planes connecting fracturing clasts across the model domain (figure 5a). However, with  $\tau/\tau_y = 0.66$ , only 34% of clast material is failing (figure 5b), as with  $\tau/\tau_y = 0.44$  if the viscosity ratio is  $10^3$ . This implies a relatively sharp change from frictional–viscous behaviour with  $\tau/\tau_y = 0.66$  to frictional at  $\tau/\tau_y = 0.88$  (figure 5a,b), as also indicated by a steepening of the % frictional deformation vs  $\tau/\tau_y$  curve in figure 5d. Reducing  $\tau/\tau_y$  to 0.44 with a viscosity ratio of 10 leaves only 1% of clast material fracturing, i.e. the shear zone is basically entirely viscous (figure 5c).

Overall, clast fracturing and therefore visco-frictional interplay increases with increasing viscosity contrast, when  $0 < \tau/\tau_y < 1$ . For a viscosity ratio of 10 the behaviour is uniformly viscous for  $\tau/\tau_y < 0.4$ , whereas for viscosity contrasts of  $10^2$  and  $10^3$ , some very minor frictional behaviour is seen at  $\tau/\tau_y = 0.22$  (figure 5d). As  $\eta_s/\eta_w$  increases, the transition zone covers a greater range of  $\tau/\tau_y$  values (figure 5e), because stress concentration in the competent bodies brings them closer to frictional yield [97,101], and the  $\tau/\tau_y$  at which frictional deformation ceases to dominate decreases. The transitions between the deformation regimes also occur at lower  $\tau/\tau_y$  ratios if  $\eta_s/\eta_w$  increases, because of this stress concentration. The transitions are likely similar at viscosity ratios  $> 10^3$ , based on the decreasing spacing of the curves in figure 5d.

Deformation style can be characterized by proportion of clast failure, as across the models 34% frictional failure appears to allow local fracturing that can only link between a few clasts (figures 4e and 5b); 63% clast failure leads to fractures connecting across the bulk or all of the model domain (figure 4c). Accordingly, we consider the bulk deformation viscous, and frictional deformation restricted to rare and very local, short length-scale deformation if less than 30% of clast material is yielding. On the other hand, if more than 60% of the clast material is yielding, then through-going fractures accommodating frictional sliding would not need to overcome barriers of clast and/or matrix material far from failure. The intermediate case, 30–60% clast material yielding, can be considered a transitional state where local fractures develop, can link between clasts and clusters of clasts, but are limited in length-scale and rarely span the model domain. These values clearly depend on geometry and clast shape; however, we plot types of deformation in figure 5e to demonstrate the shape of the viscous, frictional and frictional–viscous fields that arise from the models in  $\tau/\tau_y$  versus  $\eta_s/\eta_w$  space. For the end-member where  $\eta_s/\eta_w = 1$ , the change from frictional to viscous deformation occurs when  $\tau/\tau_y < 1$  and there is no transition zone, because there is no static stress concentration.

## 6. Model application

The models presented above consider a fault zone comprising interconnected viscously weak material surrounding stronger visco-frictional lenses. This geometry can be seen as representative for scales ranging from mineral clasts in gouges, as seen within fault cores or in laboratory experiments, through to anastomosing schistose or phyllonitic shear zones separating relatively intact, km-scale rigid wall rock lenses. Thus, we suggest the conceptual models connecting viscosity contrast and  $\tau/\tau_y$  to bulk fault behaviour can be applied to a range of settings and scales. Detailed applications are beyond the scope of this conceptual paper, however, we present some thoughts and a simple illustrative application.

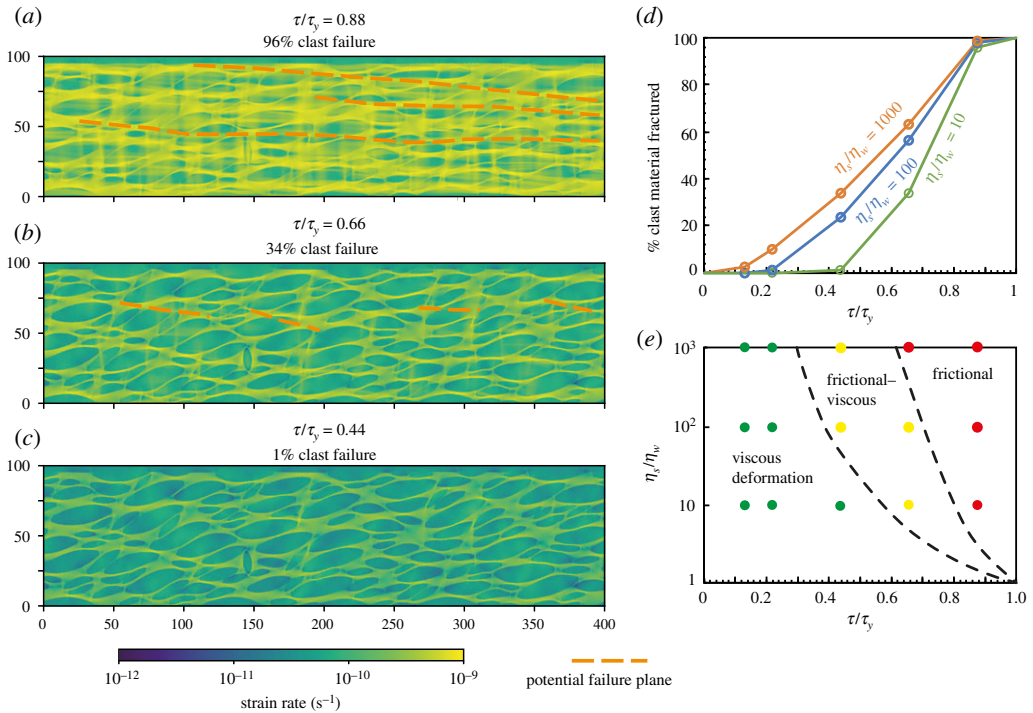


**Figure 5.** Plots of strain rate distribution within a linear-viscous shear zone where the viscosity ratio between clasts and matrix is 10. As in figure 4, the models are run at different ratios of driving stress ( $\tau$ ) to frictional yield strength ( $\tau_y$ ) of the competent phase, however, here the viscosity ratio is two orders of magnitude smaller. When  $\tau/\tau_y$  approaches 1 (a), 96% of clasts are yielding and frictional deformation dominates. There are multiple, potential through-going failure planes with lengths across the model domain. Compare this to a small  $\tau/\tau_y$  where here only 1% of clasts are failing frictionally (c), as opposed to 1/3 in the models with viscosity ratio of  $10^3$ . In the intermediate case (b), only 34% of clasts are yielding, so that there is limited potential for short, discrete fractures to form, linking only few fracturing clasts through the matrix material. The data plots shown here, those in figure 4 and additional model runs are summarized in (d), whereas combined effects of  $\tau/\tau_y$  and the viscosity ratio  $\eta_s/\eta_w$  is illustrated in (e). In (e), points show where models were run, and depict viscous (less than 30% competent material fracturing), frictional-viscous (30–60% competent material fracturing) and frictional (greater than 60% competent material fracturing), respectively. Black dashed lines approximate fields by linear interpolation between calculated points. (Online version in colour.)

### (a) Depth-dependence of frictional versus viscous deformation

We can use our two-phase numerical models (figures 4 and 5) to explore the dynamics that may control the depth-dependence of the ratio of frictional to viscous behaviour (figure 3). The models were used to predict the degree of visco-frictional interaction, based on the ratios of  $\eta_s/\eta_w$  and  $\tau/\tau_y$ . These ratios will both change with depth, depending on the depth-dependence of material properties and effective stress state. We will calculate how these ratios are expected to vary for a particular tectonic profile and subsequently map the visco-frictional regimes to depth ranges.

Conceptually, consider variations in the proportion of competent fault rocks fracturing as a function of depth for a range of viscosity ratios. These are plotted in figure 6a, where the solid, grey curves will always have same shape but will be translated shallower or deeper depending on  $\tau/\tau_y$ . Deeper than a uniformly frictional regime, a transitional zone occurs where the volume fraction of frictional failure decreases with depth. This decrease in fracturing is a result of frictional strength increasing whereas increasingly efficient viscous flow occurs in interconnected incompetent material. As depth increases, viscosity becomes progressively lower relative to a higher frictional yield strength, and at some depth shear is entirely viscous, and any

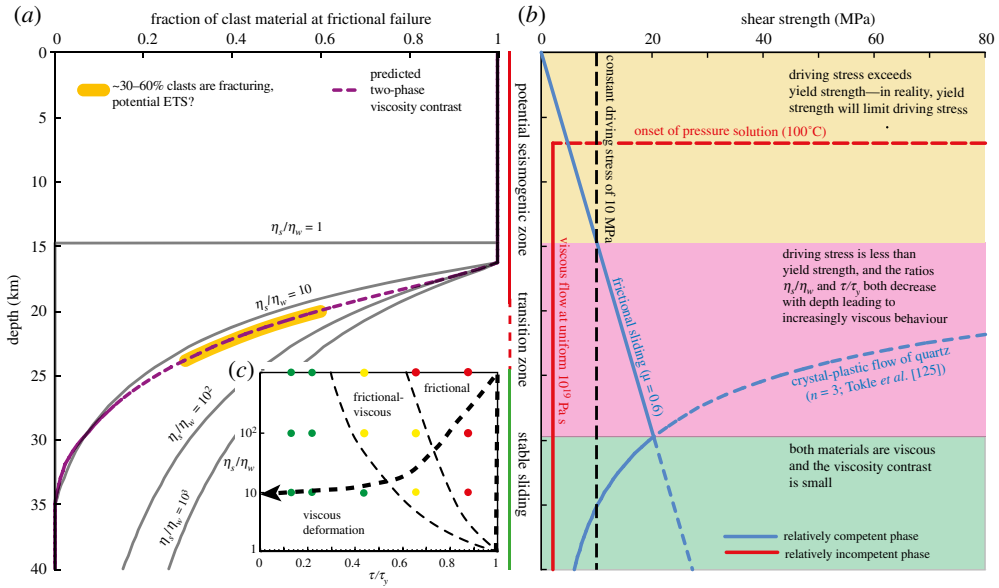


**Figure 6.** Illustrative example of strength and deformation mode in a two-phase fault zone. In (a) the fraction of competent material at frictional yield is plotted against depth for various viscosity contrasts ( $\eta_s/\eta_w$ ). (b) shows the specific example used, which is a simplified subduction thrust, involving a weak phase (red line) with viscosity  $10^{19}$  Pa s deforming by pressure solution at temperatures above  $100^\circ\text{C}$ , and a competent phase (solid blue line) controlled by Byerlee friction and a quartz flow law [125]. The black dashed line shows a driving stress of 10 MPa. Inset (c) depicts the approximate path of subducting rocks with increasing depth along the subduction interface in the deformation style map presented in figure 5e. (Online version in colour.)

competent material is too frictionally strong relative to bulk strength for any frictional failure to occur. This line of argument, however, assumes a uniform fluid overpressure—it is important to remember that at any depth, if frictional yield can be reduced sufficiently, the proportion of material undergoing frictional failure will increase markedly. Note that this depth variation in deformation is comparable to that well established from geological observations (e.g. figure 3).

### (b) A simple example: the base of the subduction thrust seismogenic zone

We now calculate a specific viscosity contrast profile example, and plot the fraction of competent material undergoing frictional failure against depth (figure 6a), based on extrapolating between models as those shown in figures 4 and 5. Mapping viscosities to depth and fraction of material fracturing (dependent on  $\tau/\tau_y$ ; figure 5d) is based on subduction-like conditions, including a near-lithostatic pore fluid factor ( $\lambda = \text{pore fluid pressure/vertical stress}$ ) of 0.9, clast friction  $\mu = 0.6$ , low driving stress of 10 MPa, and thermal gradient of  $15^\circ\text{C km}^{-1}$ . As the bulk rheology changes with depth, the constant driving stress is a simplification that implies a varying strain-rate at depth if tectonic slip is approximately uniform. If viscosity decreases with increasing temperature, as expected in a purely viscous regime, then the constant stress assumption implies strain localization and decreasing shear zone width with depth. On the other hand, shear zone width may be buffered by the yield strength of the undeformed wall rocks [126], which corresponds to shear zone widening with depth below the brittle–ductile transition, consistent with figure 1a. Such widening would also occur in a visco-frictional shear zone if increasing frictional strength has a greater effect on bulk strength than decreasing viscosity. Separating these models and further assessing the validity of the constant stress assumption could be a subject of future study. We assume the weakest component can deform by pressure solution, with a constant viscosity of  $10^{19}$  Pa s, where  $T \geq 100^\circ\text{C}$  and pressure solution is efficient in quartz; at this temperature,

frictional resistance is still less than 10 MPa at the given conditions, and a sharp frictional–viscous transition occurs somewhat deeper for  $\eta_s/\eta_w = 1$  where  $\tau_y$  drops below  $\tau$ . The onset of pressure solution will be more gradual than this T-dependent onset of a constant, low viscosity implies, leading to a broader transition zone in reality than in our models. For  $\eta_s/\eta_w > 1$ , total clast failure can occur when  $\tau/\tau_y < 1$ , such that the onset of some viscous deformation is seen a few kilometres deeper. Below this, as illustrated also in figures 4 and 5, a relatively sharp change from dominantly frictional to dominantly viscous deformation is seen for  $\eta_s/\eta_w = 10$ . For greater  $\eta_s/\eta_w$ , however, local stress amplification leads to a mixed frictional–viscous behaviour over a substantial depth range of up to tens of kilometres.

In a simplified view, the likely heterogeneous subduction thrust comprises weak, phyllosilicate-rich materials representing pelitic sediment and/or altered, hydrated oceanic crust [127], mixed with more competent materials such as sandy or cherty sediment layers and/or basaltic oceanic crust [64]. Although there are certainly depth-variations in the strength of the weak component, over our depths of interest we consider these small compared to competency contrasts, and use a constant, low, Newtonian viscosity to represent pressure-solution creep (figure 6*b*). Consider this weak component mixed with a quartz-dominated rheology, also plotted in (figure 6*b*). This competent quartz rheology is derived based on crystal plastic flow in quartz [125], assuming a constant, relatively slow, clast strain-rate of  $10^{-13} \text{ s}^{-1}$ , such that the clast viscous strength is conservatively underestimated. Then a viscosity ratio can be extracted from these two lithologies and shown as a function of depth (figure 6*a,b*).

The viscosity contrast is greatest at the onset of pressure solution, but at this depth, frictional yield is still relatively easy and a major proportion of deformation is therefore frictional (figure 6*a,b*). In other words,  $\tau/\tau_y = 1$ , and therefore all deformation is frictional independently of viscosity contrast. With increasing depth, frictional yield becomes more difficult, but for  $\eta_s/\eta_w > 10^2$ , and as long as  $\tau/\tau_y > \sim 0.6$  there is likely to still be through-going frictional failure (figure 4). However, as  $\eta_s/\eta_w$  decreases to  $10 < \eta_s/\eta_w < 10^2$  and  $\tau/\tau_y$  becomes smaller as  $\tau_y$  increases, there is a depth range where a fraction of 0.3 to 0.6 of the more competent material is fracturing (figure 6*a,c*). By comparison to figures 4 and 5, the top of this depth range may have some through-going frictional planes, but as the competence of the stronger phase decreases, these become shorter and less important in accommodating displacement. Frictional slip propagating from one block at frictional failure and through surrounding matrix would have to overcome the stress deficit of the matrix and/or adjacent blocks far from failure, potentially limiting rupture lengths to the length scale of one block (less than 100 m order; [128]). This may be comparable to the inferred decrease in stress and length-scale of low frequency earthquakes that occur within ETS in Cascadia [129,130], and the mixed behaviour of slow slip and tremor in general—where low frequency earthquakes may represent smaller-scale frictional deformation embedded within a fault deforming aseismically [131]. We make a jump here, assuming our visco-frictional deformation may lead to slow slip; we do not know if that is the case, but it is a tempting comparison given the coincidence between our predicted mixed behaviour and that seen in subduction margins hosting ETS. This comparison is compatible with slow earthquakes as self-driven frictional instabilities that have large nucleation length scales relative to the dimension of the fault hosting them (the potential frictional failure planes within our model shear zone) [132–134]. The potential for such transients to grow into larger instabilities will depend on their stress drop overcoming the shear resistance of the surrounding shear zone, which will be easier if the background stress approaches local fault strength [29]. Observation of increased moment rate during coalescence of slow slip events in Cascadia also implies that interacting instabilities have the potential of overcoming the dampening effect of intervening frictionally stable fault material [135].

The exact depth range where we predict a mixed behaviour with decreasing brittle behaviour with depth depends critically on parameters such as driving stress, fluid pressure and strain rate, but is consistently where the viscosity ratio is at least on the order of  $10^1$  to  $10^3$ , and  $0.3 < \tau/\tau_y < 0.6$ , in the transition zone from frictional to viscous deformation (e.g. figure 6*c*) as is commonly observed. Below this zone, which is likely a very narrow depth range if  $\eta_s/\eta_w$  is

10 or less,  $\eta_s/\eta_w$  approaches one and  $\tau/\tau_y$  approaches zero, such that viscous creep dominates unless local conditions, likely very high fluid pressures, allows very local frictional failure. Such local, potential instabilities will be dampened by surrounding viscous material and suppressed by a large nucleation length scale; however, unstable slip may occur if fault weakening by fluid pressurization overcomes velocity strengthening [136]—and this has been suggested previously as a mechanism for ETS spatially separated from the frictional–viscous transition [102].

We focused here on the base of the subduction interface seismogenic zone. If aseismic slip at the updip end of the seismogenic zone also involves some component of viscous deformation, then our assumption of a sharp,  $T$ -dependent onset of pressure solution at 100°C hides any shallower, near-trench effects of mixed frictional–viscous or seismic–aseismic deformation. Such shallow, visco-frictional deformation may occur in some subduction zones, particularly where carbonates make up a considerable proportion of the incoming sediment sequence [137,138]. We also recall that within the shallow, dominantly frictional regime, variations in consolidation, porosity, fluid pressure or material properties in time and space may add further heterogeneity than what we model here, even in the absence of a viscous component [47]. We highlight the shallow portion of subduction zones as a target for future study.

## 7. Is complex fault zone behaviour a reflection of rheological heterogeneity?

There appears to be a broad agreement among structural geologists that fault zone heterogeneity gives rise to a range of deformation styles, and a common co-existence of brittle and ductile structures [48,54,55,69,77,80,91–93,98,128]. However, because heterogeneity of some magnitude is present at some scale in just about every rock outcrop, a question remains of how to quantify heterogeneity, and to what extent the rheological heterogeneity inferred from the rock record reflects the heterogeneity in slip style observed by geophysical techniques in active fault zones [5,40,41,43,44,131]. One approach is to consider heterogeneity as the strength ratio between co-existing materials, and their geometrical distribution [77,91]. This, however, has limitations. If the stronger phase is very far from failure and not forming an interconnected network, it will accommodate little deformation and the weaker phase controls rheology. Similarly, if the stronger phase is very close to failure and there is insufficient interconnected weak material for the strong phase to be rheologically insignificant, it likely controls rheology, with fractures propagating through the weaker phase however easily it may deform viscously. These effects have been considered before [77,89,91], and were illustrated here in (figure 5e). There is also the case of a competent phase close to failure, but in low volumetric proportions. Rupture propagation is then limited if the volume of matrix in between blocks is too large and experiencing a background stress far below its frictional yield [29,96,115]. We add here, that although one competent block is at failure, the adjacent one might not be, depending on stress heterogeneity or local weakening by, for example, fluid pressure. Stress heterogeneity and local stress amplification is also reduced at small fractions of competent material [101], and thus the frictional–viscous regime may be narrow if weak, relatively viscous materials dominate volumetrically. These potential heterogeneities in  $\tau/\tau_y$  are analogous to frictional variation providing barriers in dynamic rupture models of rough faults [139,140]—in that a variable frictional yield will make the fault closer to failure in some areas compared to others. In our model, the barriers effectively disappear when either the driving stress or pore pressure is very high ( $\tau/\tau_y \rightarrow 1$ ), as also occurs in the rupture models.

Our models in figures 4 and 5 have a high clast/matrix volume ratio (61%) such that they best represent an anastomosing shear zone network encompassing relatively high viscosity lenses. From a range of geological observations, we suggest that heterogeneity varies with depth, and arises from a range of processes including diagenesis, the degree to which pressure solution accommodates creep in the seismogenic zone, and the strain rates that can be accommodated by diffusion and dislocation creep in different materials. We suggest that the two basic, general, controls on bulk deformation are the contrast in deformation behaviour between co-existing fault rocks, and how far the bulk driving stress is from frictional yield. Strength contrast alone is not a sufficient measure of heterogeneity, if the aim is to determine the bulk frictional–viscous

deformation style of a fault or shear zone. For our models, viscosity ratios of 10 and 1000 give depth ranges 3 and 10 km wide, respectively, where  $\tau/\tau_y$  ratios are high and frictional and viscous deformation modes co-occur as a result of stress amplification in the stronger phase, independently of the source of heterogeneity. This depth range of visco-frictional behaviour can be shifted up/down dynamically, depending on  $\tau$  and/or fluid pressure, which may both vary substantially. Observed variations in depths of SSEs and LFEs, deemed representative of a transitional regime, may be determined by these stress and fluid pressure variations, without having to invoke variation in rheology or geothermal gradient.

## 8. Conclusion

Although geological and rheological heterogeneity is pointed out in an increasing array of fault zones in several tectonic settings, the magnitude and length scale of such heterogeneity varies. To what extent can 'heterogeneity' in material properties be measured, quantified and tied to heterogeneity in fault zone deformation? We propose that, at the first order, fault slip style in a heterogeneous tabular fault zone is controlled by a combination of viscosity contrast and the ratio,  $\tau/\tau_y$ , of bulk driving stress to frictional yield strength.

In this conceptual model, earthquakes require the frictional yield to be reached, and steady viscous flow requires conditions far from the frictional yield, independently of fault zone viscosity contrasts. Intermediate slip speeds may arise when driving stress is sufficient to arise local frictional failure by stress amplification, but this failure is limited in length-scale by surrounding viscously deforming media and heterogeneity of clast stresses (and/or strengths). The conditions where this is likely cover a larger range of  $\tau/\tau_y$  at greater viscosity contrast.

Frictional deformation is more difficult and reliant upon local stress concentrations near the frictional–viscous transition, and this is consequently also where the models presented here predict a zone of intermediate and mixed deformation style. At greater depths, viscosity ratios are small and driving stress far from frictional yield, such that frictional sliding and mixed transitional behaviour is unlikely, but possible in the presence of high to extreme local fluid overpressures.

Considering the variation in fault slip style with depth in some subduction and strike slip zones, and the numerical models presented here, intermediate fault slip speeds as seen in tremor and slow slip may correspond to slip in highly heterogeneous stress fields that may arise from  $\tau/\tau_y$  ratios that are intermediate between low values suppressing frictional yield and high values allowing through-going frictional failure. The exact values depend on viscosity contrast, but lead to fractures limited by viscous, weak matrix but locally allowed to nucleate by an ability for more competent lenses to flow or fracture. This is easier over a larger depth range at higher viscosity contrast, as otherwise, the bulk rheology will tend towards either fracture or viscous flow.

**Data accessibility.** The open-source geodynamic code Underworld is available at <http://www.underworldcode.org>, and model parameters required to replicate the results are detailed in the manuscript and in [97].

**Authors' contributions.** Å.F. conceived of and designed the study with input from A.B., and drafted the manuscript and figures 1, 2 and 3. A.B. performed the modelling, generated figures 4 and 5, and reviewed the manuscript. Both authors contributed to figure 6, based on A.B.'s models. Both authors read and approved the manuscript.

**Competing interests.** We declare we have no competing interests.

**Funding.** This project has received funding from the European Research Council (ERC) under the European Union's Horizon 2020 research and innovation programme (Starting Grant agreement 715836 'MICA').

**Acknowledgements.** The authors thank the organizers and participants in the Royal Society meeting on 'Understanding earthquakes using the geological record' for fruitful and thought-provoking discussions. Ongoing support from the ARCCA Hawk computing cluster (Cardiff University) is as always appreciated and the cluster was used for all numerical calculations. We acknowledge the support of the Supercomputing Wales project, which is part-funded by the European Regional Development Fund (ERDF) via Welsh Government. Some inspiration for this study arose from Steve James' MEdSci thesis at Cardiff University, and from

## References

1. Lay T, Kanamori H, Ruff L. 1982 The asperity model and the nature of large subduction zone earthquakes. *Earthq. Predict. Res.* **1**, 3–71.
2. Faulkner DR, Lewis AC, Rutter EH. 2003 On the internal structure and mechanics of large strike-slip fault zones: field observations of the Carboneras fault in southeastern Spain. *Tectonophysics* **367**, 235–251. (doi:10.1016/S0040-1951(03)00134-3)
3. Chlieh M, Avouac JP, Sieh K, Natawidjaja DH, Galetzka J. 2008 Heterogeneous coupling of the Sumatran megathrust constrained by geodetic and paleogeodetic measurements. *J. Geophys. Res.* **113**, B05305. (doi:10.1029/2007JB004981)
4. Perfettini H *et al.* 2010 Seismic and aseismic slip on the Central Peru megathrust. *Nature* **465**, 78–81. (doi:10.1038/nature09062)
5. Peng Z, Gomberg J. 2010 An integrated perspective of the continuum between earthquakes and slow slip phenomena. *Nat. Geosci.* **3**, 599–607. (doi:10.1038/ngeo940)
6. Sibson RH. 1977 Fault rocks and fault mechanisms. *J. Geol. Soc. London* **133**, 191–213. (doi:10.1144/gsjgs.133.3.0191)
7. Brace WF, Kohlstedt DL. 1980 Limits on lithospheric stress imposed by laboratory experiments. *J. Geophys. Res.* **85**, 6248–6252. (doi:10.1029/JB085iB11p06248)
8. Scholz CH. 1988 The brittle-plastic transition and the depth of seismic faulting. *Geol. Rundsch.* **77**, 319–328. (doi:10.1007/BF01848693)
9. Scholz CH. 1998 Earthquakes and friction laws. *Nature* **391**, 37–42. (doi:10.1038/34097)
10. Chester FM, Logan JM. 1986 Implications for mechanical properties of brittle faults from observations of the Punchbowl fault zone, California. *Pure Appl. Geophys.* **124**, 79–106. (doi:10.1007/BF00875720)
11. Coward MP. 1990 Shear zones at the Laxford front, NW Scotland and their significance in the interpretation of lower crustal structure. *J. Geol. Soc. London* **147**, 279–286. (doi:10.1144/gsjgs.147.2.0279)
12. Carreras J. 2001 Zooming on Northern Cap de Creus shear zones. *J. Struct. Geol.* **23**, 1457–1486. (doi:10.1016/S0191-8141(01)00011-6)
13. Rennie SF, Fagereng A, Diener JFA. 2013 Strain distribution within a km-scale, mid-crustal shear zone: the Kuckaus Mylonite Zone, Namibia. *J. Struct. Geol.* **56**, 57–69. (doi:10.1016/j.jsg.2013.09.001)
14. Sibson RH. 1984 Roughness at the base of the seismogenic zone: contributing factors. *J. Geophys. Res.* **89**, 5791–5799. (doi:10.1029/JB089iB07p05791)
15. Handy MR, Hirth G, Bürgmann R. 2007 Fault structure and rheology from the frictional-viscous transition downward. In *Tectonic Faults: Agents of Change on a Dynamic Earth* (eds MR Handy, G Hirth, N Hovius), volume 95 of *Dahlem Workshop Report*, pp. 139–181. Cambridge, MA: MIT Press.
16. Dieterich JH. 1979 Modeling of rock friction 1. Experimental results and constitutive equations. *J. Geophys. Res.* **84**, 2161–2168. (doi:10.1029/JB084iB05p02161)
17. Ruina AL. 1983 Slip instability and state variable friction laws. *J. Geophys. Res.* **88**, 10359–10370. (doi:10.1029/JB088iB12p10359)
18. Gu JC, Rice JR, Ruina AL, Tse ST. 1984 Slip motion and stability of a single degree of freedom elastic system with rate and state dependent friction. *J. Mech. Phys. Solids* **32**, 167–196. (doi:10.1016/0022-5096(84)90007-3)
19. Marone C. 1998 Laboratory-derived friction laws and their application to seismic faulting. *Annu. Rev. Earth Planet. Sci.* **26**, 643–696. (doi:10.1146/annurev.earth.26.1.643)
20. Leeman JR, Saffer DM, Scuderi MM, Marone C. 2016 Laboratory observations of slow earthquakes and the spectrum of tectonic fault slip styles. *Nat. Commun.* **7**, 11104. (doi:10.1038/ncomms11104)
21. Reinen LA, Tullis TE, Weeks JD. 1992 Two-mechanism model for frictional sliding of serpentinite. *Geophys. Res. Lett.* **19**, 1535–1538. (doi:10.1029/92GL01388)
22. Kilgore BD, Blanpied ML, Dieterich JH. 1993 Velocity dependent friction of granite over a wide range of conditions. *Geophys. Res. Lett.* **20**, 903–906. (doi:10.1029/93GL00368)

23. den Hartog SAM, Spiers CJ. 2014 A microphysical model for fault gouge friction applied to subduction megathrusts. *J. Geophys. Res.* **119**, 1510–1529. (doi:10.1002/2013JB010580)
24. Niemeijer AR. 2018 Velocity-dependent slip weakening by the combined operation of pressure solution and foliation development. *Sci. Rep.* **8**, 4724. (doi:10.1038/s41598-018-22889-3)
25. Mair K, Marone C. 1999 Friction of simulated fault gouge for a wide range of velocities and normal stresses. *J. Geophys. Res.* **104**, 28 299–28 914. (doi:10.1029/1999JB900279)
26. Scuderi MM, Collettini C, Viti C, Tinti C, Marone C. 2017 Evolution of shear fabric in granular fault gouge from stable sliding to stick slip and implications for fault slip mode. *Geology* **45**, 731–734. (doi:10.1130/G39033.1)
27. Noda H, Lapusta N. 2013 Stable creeping fault segments can become destructive as a result of dynamic weakening. *Nature* **493**, 518–521. (doi:10.1038/nature11703)
28. Bécél A *et al.* 2017 Tsunamigenic structures in a creeping section of the Alaska subduction zone. *Nat. Geosci.* **10**, 609–613. (doi:10.1038/ngeo2990)
29. van den Ende MPA, Chen J, Niemeijer AR, Ampuero JP. 2020 Rheological transitions facilitate fault-spanning ruptures on seismically active and creeping faults. *J. Geophys. Res.* **125**, e2019JB019328. (doi:10.1029/2019JB019328)
30. Marone C, Scholz CH. 1988 The depth of seismic faulting and the upper transition from stable to unstable slip regimes. *Geophys. Res. Lett.* **15**, 621–624. (doi:10.1029/GL015i006p00621)
31. Blanpied ML, Lockner DA, Byerlee JD. 1991 Fault stability inferred from granite sliding experiments at hydrothermal conditions. *Geophys. Res. Lett.* **18**, 609–612. (doi:10.1029/91GL00469)
32. den Hartog SAM, Niemeijer AR, Spiers CJ. 2012 New constraints on megathrust slip stability under subduction zone P–T conditions. *Earth Planet. Sci. Lett.* **353**, 240–252. (doi:10.1016/j.epsl.2012.08.022)
33. den Hartog SAM, Niemeijer AR, Spiers CJ. 2013 Friction on subduction megathrust faults: beyond the illite–muscovite transition. *Earth Planet. Sci. Lett.* **373**, 8–19. (doi:10.1016/j.epsl.2013.04.036)
34. Sibson RH. 1982 Fault zone models, heat flow, and the depth distribution of earthquakes in the continental crust of the United States. *Bull. Seismol. Soc. Am.* **72**, 151–163.
35. Hyndman RD, Yamano M, Oleskevich DA. 1997 The seismogenic zone of subduction thrust faults. *Island Arc* **6**, 244–260. (doi:10.1111/j.1440-1738.1997.tb00175.x)
36. Linde AT, Gladwin M, Johnston M, Gwyther R, Bilham R. 1996 A slow earthquake sequence on the San Andreas fault. *Nature* **383**, 65–68. (doi:10.1038/383065a0)
37. Dragert H, Wang K, James TS. 2001 A silent slip event on the deeper Cascadia subduction interface. *Science* **292**, 1525–1528. (doi:10.1126/science.1060152)
38. Katsumata A, Kamaya N. 2003 Low frequency continuous tremor around the Moho discontinuity away from volcanoes in the southwest Japan. *Geophys. Res. Lett.* **30**, 20-1–20-4. (doi:10.1029/2002GL015981)
39. Shelly DR, Beroza GC, Ide S. 2007 Non-volcanic tremor and low-frequency earthquake swarms. *Nature* **446**, 305–307. (doi:10.1038/nature05666)
40. Rogers GC, Dragert H. 2003 Episodic tremor and slip on the Cascadia subduction zone: the chatter of silent slip. *Science* **300**, 1942–1943. (doi:10.1126/science.1084783)
41. Obara K, Hirose H, Yamamizu F, Kasahara K. 2004 Episodic slow slip events accompanied by non-volcanic tremors in southwest Japan subduction zone. *Geophys. Res. Lett.* **31**, L23602. (doi:10.1029/2004GL020848)
42. Davis EE, Villinger H, Sun T. 2015 Slow and delayed deformation and uplift of the outermost subduction prism following ETS and seismogenic slip events beneath Nicoya Peninsula, Costa Rica. *Earth Planet. Sci. Lett.* **410**, 117–127. (doi:10.1016/j.epsl.2014.11.015)
43. Wallace LM, Webb SC, Ito Y, Mochizuki K, Hino R, Henrys S, Schwartz SY, Sheehan AF. 2016 Slow slip near the trench at the Hikurangi subduction zone, New Zealand. *Science* **352**, 701–704. (doi:10.1126/science.aaf2349)
44. Araki E, Saffer DM, Kopf A, Wallace LM, Kimura T, Machida Y, Ide S, Davis E, IODP Expedition 365 Shipboard Scientists. 2017 Recurring and triggered slow-slip events near the trench at the Nankai Trough subduction megathrust. *Science* **356**, 1157–1160. (doi:10.1126/science.aan3120)

45. Fu Y, Freymueller JT. 2013 Repeated large Slow Slip Events at the southcentral Alaska subduction zone. *Earth Planet. Sci. Lett.* **375**, 303–311. (doi:10.1016/j.epsl.2013.05.049)
46. Liu Y, Rice JR. 2005 Aseismic slip transients emerge spontaneously in three-dimensional rate and state modeling of subduction earthquake sequences. *J. Geophys. Res.* **110**, B08307. (doi:10.1029/2004JB003424)
47. Saffer DM, Wallace LM. 2015 The frictional, hydrologic, metamorphic and thermal habitat of shallow slow earthquakes. *Nat. Geosci.* **8**, 594–600. (doi:10.1038/ngeo2490)
48. Cowan DS. 1985 Structural styles in Mesozoic and Cenozoic melanges in the western Cordillera of North America. *Geol. Soc. Am. Bull.* **96**, 451–462. (doi:10.1130/0016-7606(1985)96<451:SSIMAC>2.0.CO;2)
49. Festa A, Ogata K, Pini GA. 2020 Polygenetic mélanges: a glimpse on tectonic, sedimentary and diapiric recycling in convergent margins. *J. Geol. Soc. London* **177**, 551–561. (doi:10.1144/jgs2019-212)
50. Fagereng A. 2011 Geology of the seismogenic subduction thrust interface. In *Geology of the Earthquake Source: A Volume in Honour of Rick Sibson* (eds A Fagereng, VG Toy, JV Rowland), vol. 359 of *Special Publication*, pp. 55–76. London, UK: Geological Society.
51. Ujiie K, Saishu H, Fagereng A, Nishiyama N, Otsubo M, Masuyama H, Kagi H. 2018 An explanation for episodic tremor and slow slip constrained by crack-seal veins and viscous shear in subduction mélange. *Geophys. Res. Lett.* **45**, 5371–5379. (doi:10.1029/2018GL078374)
52. Cross CB, Diener JFA, Fagereng A. 2015 Metamorphic imprint of accretion and ridge subduction in the Pan-African Damara Belt, Namibia. *J. Metamorphic Geol.* **33**, 633–648. (doi:10.1111/jmg.12139)
53. Fagereng A, Diener JFA, Meneghini F, Harris C, Kvadshem A. 2018 Quartz vein formation by local dehydration embrittlement along the deep, tremorgenic subduction thrust interface. *Geology* **46**, 67–70. (doi:10.1130/G39649.1)
54. Byrne T. 1984 Early deformation in mélange terranes of the Ghost Rocks Formation, Kodiak Islands, Alaska. In *Mélanges: their Nature, Origin, and Significance* (ed. LA Raymond), vol. 198 of *Special Papers*, pp. 21–51. Geological Society of America.
55. Fisher D, Byrne T. 1987 Structural evolution of underthrust sediments, Kodiak Island, Alaska. *Tectonics* **6**, 775–793. (doi:10.1029/TC006i006p00775)
56. Ujiie K. 2002 Evolution and kinematics of an ancient décollement zone, mélange in the Shimanto accretionary complex of Okinawa Island, Ryukyu Arc. *J. Struct. Geol.* **24**, 937–952. (doi:10.1016/S0191-8141(01)00103-1)
57. Moore JC, Saffer D. 2001 Updip limit of the seismogenic zone beneath the accretionary prism of southwest Japan: an effect of diagenetic to low-grade metamorphic processes and increasing effective stress. *Geology* **29**, 183–186. (doi:10.1130/0091-7613(2001)029<0183:ULOTSZ>2.0.CO;2)
58. Hashimoto Y, Nakaya T, Ito M, Kimura G. 2006 Tectonolithification of sandstone prior to the onset of seismogenic subduction zone: evidence from tectonic mélange of the Shimanto Belt, Japan. *Geochem. Geophys. Geosyst.* **7**, Q06013. (doi:10.1029/2005GC001062)
59. Fialko Y, Sandwell D, Simons M, Rosen P. 2005 Three-dimensional deformation caused by the Bam, Iran, earthquake and the origin of shallow slip deficit. *Nature* **435**, 295–299. (doi:10.1038/nature03425)
60. Titus SJ, DeMets C, Tikoff B. 2006 Thirty-five-year creep rates for the creeping segment of the San Andreas Fault and the effects of the 2004 Parkfield earthquake: constraints from alignment arrays, continuous global positioning system, and creepmeters. *Bull. Seismol. Soc. Am.* **96**, S250–S268. (doi:10.1785/0120050811)
61. Jolivet R, Lasserre C, Doin MP, Guillaso S, Peltzer G, Dailu R, Sun J, Shen ZK, Xu X. 2012 Shallow creep on the Haiyuan Fault (Gansu, China) revealed by SAR Interferometry. *J. Geophys. Res.* **117**, B06401. (doi:10.1029/2011JB008732)
62. Wei M, Kaneko Y, Liu Y, McGuire JJ. 2013 Episodic fault creep events in California controlled by shallow frictional heterogeneity. *Nat. Geosci.* **7**, 566–570. (doi:10.1038/ngeo1835)
63. Boulton C, Niemeijer AR, Hollis CJ, Townend J, Raven MD, Kulhanek DK, Shepherd CL. 2019 Temperature-dependent frictional properties of heterogeneous Hikurangi Subduction Zone input sediments, ODP Site 1124. *Tectonophysics* **757**, 123–139. (doi:10.1016/j.tecto.2019.02.006)
64. Barnes PM *et al.* 2020 Slow slip source characterized by lithological and geometric heterogeneity. *Sci. Adv.* **6**, eaay3314. (doi:10.1126/sciadv.aay3314)

65. Chen T, Lapusta N. 2009 Scaling of small repeating earthquakes explained by interaction of seismic and aseismic slip in a rate and state fault model. *J. Geophys. Res.* **114**, B01311. (doi:10.1029/2008JB005749)
66. Tobin H, Vannucchi P, Meschede M. 2001 Structure, inferred mechanical properties, and implications for fluid transport in the décollement zone, Costa Rica convergent margin. *Geology* **29**, 907–910. (doi:10.1130/0091-7613(2001)029<0907:SIMPAI>2.0.CO;2)
67. Kinoshita M, Tobin H, Ashi J, Kimura G, Lallemand S, Screaton EJ, Curewitz D, Masago H, Moe KT, Expedition 314/315/316 Scientists. 2009 NanTroSEIZE Stage 1: Investigations of seismogenesis, Nankai Trough, Japan. In *Proceedings of the Integrated Ocean Drilling Program*, volume 314/315/316. College Station, TX: International Ocean Discovery Program.
68. Fabbri O *et al.* 2020 Deformation structures from splay and décollement faults in the Nankai Accretionary Prism, SW Japan (IODP NanTroSEIZE Expedition 316): evidence for slow and rapid slip in fault rocks. *Geochem. Geophys. Geosyst.* **21**, e2019GC008786. (doi:10.1029/2019GC008786)
69. Fagereng Å *et al.* 2019 Mixed deformation styles observed on a shallow subduction thrust, Hikurangi margin, New Zealand. *Geology* **47**, 872–876. (doi:10.1130/G46367.1)
70. Segall P, Rice JR. 1995 Dilatancy, compaction, and slip instability of a fluid-infiltrated fault. *J. Geophys. Res.* **100**, 22155–22171. (doi:10.1029/95JB02403)
71. Noël C, Passelègue FX, Giorgetti C, Violay M. 2019 Fault reactivation during fluid pressure oscillations: transition from stable to unstable slip. *J. Geophys. Res.* **124**, 10940–10953. (doi:10.1029/2019JB018517)
72. Proctor B, Lockner DA, Kilgore BD, Mitchell TM, Beeler NM. 2020 Direct evidence for fluid pressure, dilatancy, and compaction affecting slip in isolated faults. *Geophys. Res. Lett.* **47**, e2019GL086767. (doi:10.1029/2019GL086767)
73. Reid HF. 1910 *The California earthquake of April 18, 1906, The mechanics of the earthquake*, volume 2 of *Report of the State Earthquake Investigation Commission*. Carnegie institution of Washington.
74. Brace W, Byerlee JD. 1966 Stick-slip as a mechanism for earthquakes. *Science* **153**, 990–992. (doi:10.1126/science.153.3739.990)
75. Tse ST, Rice JR. 1986 Crustal earthquake instability in relation to the depth variation of frictional slip properties. *J. Geophys. Res.* **91**, 9452–9472. (doi:10.1029/JB091iB09p09452)
76. Rice JR, Ben-Zion Y. 1996 Slip complexity in earthquake fault models. *Proc. Natl Acad. Sci. USA* **93**, 3811–3818. (doi:10.1073/pnas.93.9.3811)
77. Fagereng A, Sibson RH. 2010 Melange rheology and seismic style. *Geology* **38**, 751–754. (doi:10.1130/G30868.1)
78. Imber J, Holdsworth RE, Smith SAF, Jefferies SP, Collettini C. 2008 Frictional-viscous flow, seismicity and the geology of weak faults: a review and future directions. *Geol. Soc. London Spec. Publ.* **299**, 151–173. (doi:10.1144/SP299.10)
79. Gratier JP, Gamond JF. 1990 Transition between seismic and aseismic deformation in the upper crust. In *Deformation Mechanisms, Rheology and Tectonics* (eds RJ Knipe, EH Rutter), volume 54 of *Geological Society of London Special Publication*, pp. 461–473. Geological Society of London.
80. Rowe CD, Meneghini F, Moore JC. 2011 Textural record of the seismic cycle: strain-rate variation in an ancient subduction thrust. *Geol. Soc. London Spec. Publ.* **359**, 77–95. (doi:10.1144/SP359.5)
81. Shimamoto T, Logan JM. 1981 Effects of simulated clay gouges on the sliding behavior of Tennessee sandstone. *Tectonophysics* **75**, 243–255. (doi:10.1016/0040-1951(81)90276-6)
82. Imber J, Holdsworth RE, Butler CA, Lloyd GE. 1997 Fault-zone weakening processes along the reactivated Outer Hebrides Fault Zone, Scotland. *J. Geol. Soc. London* **154**, 105–109. (doi:10.1144/gsjgs.154.1.0105)
83. Richard J, Gratier JP, Doan ML, Boullier AM, Renard F. 2014 Rock and mineral transformations in a fault zone leading to permanent creep: interactions between brittle and viscous mechanisms in the San Andreas Fault. *J. Geophys. Res.* **119**, 8132–8153. (doi:10.1002/2014JB011489)
84. Fagereng A. 2017 Subduction megathrust creep governed by pressure solution and frictional-viscous flow. *Nat. Geosci.* **10**, 51–57. (doi:10.1038/ngeo2857)
85. Rutter EH. 1976 The kinetics of rock deformation by pressure solution. *Phil. Trans. R. Soc. Lond. A* **283**, 203–219. (doi:10.1098/rsta.1976.0079)

86. Bos B, Peach CJ, Spiers CJ. 2000 Frictional-viscous flow of simulated fault gouge caused by the combined effects of phyllosilicates and pressure solution. *Tectonophysics* **327**, 173–194. (doi:10.1016/S0040-1951(00)00168-2)
87. Niemeijer AR, Spiers CJ. 2005 Influence of phyllosilicates on fault strength in the brittle-ductile transition: insights from rock analogue experiments. *Geol. Soc. London Spec. Publ.* **245**, 303–327. (doi:10.1144/GSL.SP.2005.245.01.15)
88. Ramsay JG, Graham RH. 1970 Strain variation in shear belts. *Can. J. Earth Sci.* **7**, 786–813. (doi:10.1139/e70-078)
89. Handy MR. 1990 The solid-state flow of polymineralic rocks. *J. Geophys. Res.* **95**, 8647–8661. (doi:10.1029/JB095iB06p08647)
90. Goodwin LB, Tikoff B. 2002 Competency contrast, kinematics and the development of foliations and lineations in the crust. *J. Struct. Geol.* **24**, 1065–1085. (doi:10.1016/S0191-8141(01)00092-X)
91. Handy MR, Wissing S, Streit L. 1999 Frictional-viscous flow in mylonite with varied biminerallitic composition and its effect on lithospheric strength. *Tectonophysics* **303**, 175–191. (doi:10.1016/S0040-1951(98)00251-0)
92. Druguet E, Alsop GI, Carreras J. 2009 Coeval brittle and ductile structures associated with extreme deformation partitioning in a multilayer sequence. *J. Struct. Geol.* **31**, 498–511. (doi:10.1016/j.jsg.2009.03.004)
93. Colletti C, Niemeijer A, Viti C, Smith SAF, Marone C. 2011 Fault structure, frictional properties and mixed-mode fault behavior. *Earth Planet. Sci. Lett.* **311**, 316–327. (doi:10.1016/j.epsl.2011.09.020)
94. Sibson RH. 1980 Transient discontinuities in ductile shear zones. *J. Struct. Geol.* **2**, 165–171. (doi:10.1016/0191-8141(80)90047-4)
95. Campbell LR, Menegon L, Fagereng A, Pennacchioni G. 2020 Earthquake nucleation in the lower crust by local stress amplification. *Nat. Commun.* **11**, 1322. (doi:10.1038/s41467-020-15150-x)
96. Skarbak RM, Rempel AW, Schmidt DA. 2012 Geologic heterogeneity can produce aseismic slip transients. *Geophys. Res. Lett.* **39**, L21306. (doi:10.1029/2012GL053762)
97. Beall A, Fagereng A, Ellis S. 2019 Fracturing and weakening of jammed subduction shear zones, leading to the generation of slow slip events. *Geochem. Geophys. Geosyst.* **20**, 4869–4884. (doi:10.1029/2019GC008481)
98. Behr WM, Kotowski AJ, Ashley KT. 2018 Dehydration-induced rheological heterogeneity and the deep tremor source in warm subduction zones. *Geology* **46**, 475–478. (doi:10.1130/G40105.1)
99. Stenvall CA, Fagereng A, Diener JFA. 2019 Weaker than weakest: on the strength of shear zones. *Geophys. Res. Lett.* **13**, 7404–7413. (doi:10.1029/2019GL083388)
100. Yardley BWD. 1983 Quartz veins and devolatilization during metamorphism. *J. Geol. Soc. London* **140**, 657–663. (doi:10.1144/gsjgs.140.4.0657)
101. Beall A, Fagereng A, Ellis S. 2019 Strength of strained two-phase mixtures: application to rapid creep and stress amplification in subduction zone mélange. *Geophys. Res. Lett.* **46**, 169–178. (doi:10.1029/2018GL081252)
102. Gao X, Wang K. 2017 Rheological separation of the megathrust seismogenic zone and episodic tremor and slip. *Nature* **543**, 416–419. (doi:10.1038/nature21389)
103. Rice JR. 1992 Fault stress states, pore pressure distributions, and the weakness of the San Andreas fault. In *Fault mechanics and transport properties of rocks* (eds B Evans, T Wong), pp. 475–503. San Diego, CA: Academic Press.
104. Suppe J. 2014 Fluid overpressure and strength of the sedimentary upper crust. *J. Struct. Geol.* **69**, 481–492. (doi:10.1016/j.jsg.2014.07.009)
105. Fagereng A, Diener JFA, Ellis S, Remitti F. 2018 Fluid-related deformation processes at the up- and downdip limits of the subduction thrust seismogenic zone: what do the rocks tell us? In *Geology and Tectonics of Subduction Zones: A Tribute to Gaku Kimura* (eds T Byrne, MB Underwood, D Fisher, L McNeill, D Saffer, K Ujiie, A Yamaguchi), vol. 534 of *Geological Society of America Special Paper*, pp. 187–215. Geological Society of America.
106. den Hartog SAM, Spiers CJ. 2013 Influence of subduction zone conditions and gouge composition on frictional slip stability of megathrust faults. *Tectonophysics* **600**, 75–90. (doi:10.1016/j.tecto.2012.11.006)

107. Chen J, Spiers CJ. 2016 Rate and state frictional and healing behavior of carbonate fault gouge explained using microphysical model. *J. Geophys. Res.* **121**, 8642–8665. (doi:10.1002/2016JB013470)
108. Rimstidt JD, Barnes HL. 1980 The kinetics of silica-water reactions. *Geochim. Cosmochim. Acta* **44**, 1683–1699. (doi:10.1016/0016-7037(80)90220-3)
109. Rimstidt JD. 1997 Quartz solubility at low temperatures. *Geochim. Cosmochim. Acta* **61**, 2553–2558. (doi:10.1016/S0016-7037(97)00103-8)
110. Bos B, Spiers CJ. 2002 Frictional-viscous flow of phyllosilicate-bearing fault-rock: microphysical model and implications for crustal strength profiles. *J. Geophys. Res.* **107**, 2028. (doi:10.1029/2001JB000301)
111. Niemeijer AR, Spiers CJ. 2007 A microphysical model for strong velocity weakening in phyllosilicate-bearing fault gouges. *J. Geophys. Res.* **112**, B10405. (doi:10.1029/2007JB005008)
112. Verberne B, Niemeijer AR, De Bresser JHP, Spiers CJ. 2015 Mechanical behavior and microstructure of simulated calcite fault gouge sheared at 20–600°C: implications for natural faults in limestones. *J. Geophys. Res.* **120**, 8169–8196. (doi:10.1002/2015JB012292)
113. Chen J, Niemeijer AR. 2017 Seismogenic potential of a gouge-filled fault and the criterion for its slip stability: constraints from a microphysical model. *J. Geophys. Res.* **122**, 9658–9688. (doi:10.1002/2017JB014228)
114. Ando R, Takeda N, Yamashita T. 2012 Propagation dynamics of seismic and aseismic slip governed by fault heterogeneity and Newtonian rheology. *J. Geophys. Res.* **117**, B11308.
115. Luo Y, Ampuero JP. 2018 Stability of faults with heterogeneous friction properties and effective normal stress. *Tectonophysics* **733**, 257–272. (doi:10.1016/j.tecto.2017.11.006)
116. Hayman NW, Lavier LL. 2014 The geologic record of deep episodic tremor and slip. *Geology* **42**, 195–198. (doi:10.1130/G34990.1)
117. Webber S, Ellis S, Fagereng A. 2018 ‘Virtual shear box’ experiments of stress and slip cycling within a subduction interface mélange. *Earth Planet. Sci. Lett.* **488**, 27–35. (doi:10.1016/j.epsl.2018.01.035)
118. Moresi L, Quenette S, Lemiale V, Mériaux C, Appelbe B, Mühlhaus HB. 2007 Computational approaches to studying non-linear dynamics of the crust and mantle. *Phys. Earth Planet. Inter.* **163**, 69–82. (doi:10.1016/j.pepi.2007.06.009)
119. Lambe TW, Whitman RV. 1969 *Soil mechanics*. Series in Soil Engineering. New York, NY: John Wiley and Sons.
120. Sawyer DE, Flemings PB, Buttles J, Mohrig D. 2012 Mudflow transport behavior and deposit morphology: role of shear stress to yield strength ratio in subaqueous experiments. *Mar. Geol.* **307–310**, 28–39. (doi:10.1016/j.margeo.2012.01.009)
121. Meyer GG, Brantut N, Mitchell TM, Meredith PG. 2019 Fault reactivation and strain partitioning across the brittle-ductile transition. *Geology* **47**, 1127–1130. (doi:10.1130/G46516.1)
122. Eshelby JD. 1959 The elastic field outside an ellipsoidal inclusion. *Proc. R. Soc. Lond. A* **252**, 561–569. (doi:10.1098/rspa.1959.0173)
123. Misra S, Mandal N. 2007 Localization of plastic zones in rocks around rigid inclusions: insights from experimental and theoretical models. *J. Geophys. Res.* **112**, B09206. (doi:10.1029/2006JB004328)
124. Peyrat S, Olsen K, Madariaga R. 2001 Dynamic modeling of the 1992 Landers earthquake. *J. Geophys. Res.* **106**, 26467–26482. (doi:10.1029/2001JB000205)
125. Tøkle L, Hirth G, Behr WM. 2019 Flow laws and fabric transitions in wet quartzite. *Earth Planet. Sci. Lett.* **505**, 152–161. (doi:10.1016/j.epsl.2018.10.017)
126. Platt JP, Behr WM. 2011 Lithospheric shear zones as constant stress experiments. *Geology* **39**, 127–130. (doi:10.1130/G31561.1)
127. Tulley CJ, Fagereng A, Ujiie K. 2020 Hydrous oceanic crust hosts megathrust creep at low shear stresses. *Sci. Adv.* **6**, eaba1529. (doi:10.1126/sciadv.aba1529)
128. Kotowski AJ, Behr WM. 2019 Length scales and types of heterogeneities along the deep subduction interface: insights from exhumed rocks on Syros Island, Greece. *Geosphere* **15**, 1038–1065. (doi:10.1130/GES02037.1)
129. Wech AG, Creager KC. 2011 A continuum of stress, strength and slip in the Cascadia subduction zone. *Nat. Geosci.* **4**, 624–628. (doi:10.1038/ngeo1215)

130. Sweet JR, Creager KC, Houston H, Chestler SR. 2019 Variations in Cascadia low-frequency earthquake behaviour with downdip distance. *Geochem. Geophys. Geosyst.* **20**, 1202–1217. (doi:10.1029/2018GC007998)
131. Chestler SR, Creager KC. 2017 A model for low-frequency earthquake slip. *Geochem. Geophys. Geosyst.* **18**, 4690–4708. (doi:10.1002/2017GC007253)
132. Rubin AM. 2008 Episodic slow slip events and rate-and-state friction. *J. Geophys. Res.* **113**, B11414. (doi:10.1029/2008JB005642)
133. Hawthorne JC, Rubin AM. 2013 Laterally propagating slow slip events in a rate and state friction model with a velocity-weakening to velocity-strengthening transition. *J. Geophys. Res.* **118**, 3785–3808. (doi:10.1002/jgrb.50261)
134. van den Ende MPA, Chen J, Ampuero JP, Niemeijer AR. 2018 A comparison between rate-and-state friction and microphysical models, based on numerical simulations of fault slip. *Tectonophysics* **733**, 273–295. (doi:10.1016/j.tecto.2017.11.040)
135. Bletery Q, Nocquet JM. 2020 Slip bursts during coalescence of slow slip events in Cascadia. *Nat. Commun.* **11**, 2159. (doi:10.1038/s41467-020-15494-4)
136. Scuderi MM, Collettini C, Marone C. 2017 Frictional stability and earthquake triggering during fluid pressure stimulation of an experimental fault. *Earth Planet. Sci. Lett.* **477**, 84–96. (doi:10.1016/j.epsl.2017.08.009)
137. Ikari MJ, Niemeijer AR, Spiers CJ, Kopf AJ, Saffer DM. 2013 Experimental evidence linking slip instability with seafloor lithology and topography at the Costa Rica convergent margin. *Geology* **41**, 891–894. (doi:10.1130/G33956.1)
138. Leah H, Fagereng A, Meneghini F, Morgan JK, Savage HM, Wang M, Bell RE, Ikari MJ. 2020 Mixed brittle and viscous strain localisation in pelagic sediments seaward of the Hikurangi margin, New Zealand. *Tectonics* **39**, e2019TC005965. (doi:10.1029/2019TC005965)
139. Ripperger J, Ampuero JP, Mai PM, Giardini D. 2007 Earthquake source characteristics from dynamic rupture with constrained stochastic fault stress. *J. Geophys. Res.* **112**, B04311. (doi:10.1029/2006JB004515)
140. Fang Z, Dunham EM. 2013 Additional shear resistance from fault roughness and stress levels on geometrically complex faults. *J. Geophys. Res.* **118**, 3642–3654. (doi:10.1002/jgrb.50262)